Existence of positive skewness of velocity gradient in early transition

H. K. Zhao [1], Y. W. Liu,[1] L. Shao [2], L. Fang [3,4,*] and M. Dong[5,†]

[1]*National Key Laboratory of Science and Technology on Aero-Engine Aero-Thermodynamics, School of Energy and Power Engineering, Beihang University, Beijing 100191, China*

[2]*LMFA, CNRS, Ecole Centrale de Lyon–Université de Lyon, 69130 Ecully, France*

[3]*Laboratory of Complex Systems, Ecole Centrale de Pékin, Beihang University, Beijing 100191, China*

[4]*Beihang Hangzhou Innovation Institute Yuhang, Hangzhou 310034, China*

[5]*State Key Laboratory of Nonlinear Mechanics, Institute of Mechanics, Chinese Academy of Sciences, Beijing 100190, China*

(Received 17 May 2021; accepted 13 October 2021; published 25 October 2021)

The present study uses direct numerical simulations to calculate two different transitional flows from laminar flow to turbulence, that is, the two-scale wake flow and the two-dimensional Reyleigh-Taylor unstable flow, respectively. Both results show that the skewness of the longitudinal velocity gradient, S_k, can become positive in the early transition stage, which is beyond our expectation since the turbulent equilibrium state always implies negative values of S_k. These phenomena are explained analytically by considering only two dominant Fourier modes with harmonic relations. It is illustrated that the sign of S_k is not only affected by the amplitudes of the perturbation velocities, but also related to their phases. We expect that the present results will be helpful for understanding the formation of turbulent equilibrium state and for constructing a new measurable criterion of the transition onset.

DOI: 10.1103/PhysRevFluids.6.104608

I. INTRODUCTION

Turbulence is usually regarded as a chaotic dynamic system characterized by the presence of various temporal and spacial scales. A distinguished phenomenon of turbulence is the interscale energy transfer. When energy is transferred from large to small scales, it is referred to as the forward transfer or energy cascade [1]; by contrast, the inverse energy cascade, also called energy backscatter, refers to the energy transfer from small to large scales. In physical space, the interscale energy transfer can be quantitatively represented by involving the concept of the third-order moments of the velocity gradient or velocity increment [2,3]. Specifically, the skewness of the longitudinal velocity gradient is defined as

$$S_k := \left\langle \left(\frac{\partial u}{\partial x}\right)^3 \right\rangle \Big/ \left\langle \left(\frac{\partial u}{\partial x}\right)^2 \right\rangle^{3/2}, \tag{1}$$

with x being the longitudinal direction, u the fluctuation of longitudinal velocity component, and $\langle\rangle$ the ensemble averaging. In three-dimensional statistically steady and fully developed turbulence, it is already known that S_k is a negative constant which weakly depends on Reynolds number [4–7]. The negative sign corresponds to the forward interscale energy transfer, which supports Kolmogorov's 1941 theory [1,2]. In turbulence, the change of the sign of S_k or nonconstant

*Corresponding author: le.fang@buaa.edu.cn

†Corresponding author: dongming@imech.ac.cn

value of S_k means that the flow is not in a statistically equilibrium state, which corresponds to a self-organizing process among various turbulence scales. For example, a Gaussian random field yields null S_k; an incompressible isotropic two-dimensional turbulence also leads to null S_k (see Refs. [8,9] for discussions); and in some typical initial conditions the energy transfer is suppressed in a very short time period [10,11], while S_k is accordingly near zero. We also observed positive S_k when reversing the velocities in a fully developed three-dimensional turbulence [12,13], which leads to a strong nonequilibrium procedure afterwards [14–16]. Indeed, positive S_k in real turbulence, such as flow in air compressors [17], usually indicates a signal of energy backscatter.

In a recent direct numerical simulation (DNS), we found that in the early transition stage of spatial-developing channel flow, the value of S_k can be unexpectedly positive [9]. This fact could be surprising because intuitively we should expect S_k to decrease monotonically from 0 (Gaussian random field) to the negative constant (turbulence), as predicted in turbulence closure theories [4]. The explanation of this phenomenon in Ref. [9] is an incomplete tentative. Moreover, we do not even know if this positive S_k is universal or occasional. In this sense, we attempt to carry out more investigations to reveal the behavior of S_k. We will report the statistical results of two numerical configurations which respectively correspond to different scenarios of transition to turbulence to argue that the phenomenon of positive S_k can occur in the early transition phase. Analytical approximations and modelings are then presented to better explain these phenomena. Note that the present observations only consider the skewness of streamwise velocity gradient as a characteristic quantity in early transition of anisotropic flows without involving any local isotropy assumption on velocity gradient moments.

In the following sections, we will present two different transition flows respectively: a two-scale wake in Sec. II and a two-dimensional Reyleigh-Taylor flow in Sec. III. Both cases will show positive S_k in the early transition stage. Analytical models then will be introduced to explain this phenomenon, in Secs. II C and III C, respectively. Discussion of the underlying mechanism and the perspectives will be given in Sec. IV.

II. TRANSITION IN A TWO-SCALE WAKE

In order to investigate the phenomenon of positive skewness in early transition, in this section we design a numerical experiment for a two-scale wake. This case is an extreme simplification of the wake transition and can also be interpreted as the experiment of a two-scale grid-generated turbulence. Only two Fourier modes with harmonic relations are introduced as the inlet condition, which simplifies the description of the wake flow and enables the analytical approximation in the subsections.

A. Simulation settings

We consider a perfect-gas uniform flow with infinitesimal noises propagating through a semipermeable membrane panel of two-scale grids, which generates vorticities and fluctuations with different scales in the wake of the panel, leading to transition to turbulence eventually. The flow field is described in the three-dimensional Cartesian coordinate system (x_1, x_2, x_3), with x_1 along the streamwise direction and the origin o at the panel. For a selected cuboid computational domain, $[-0.4L, 16L] \times [0, 2L] \times [0, 2L]$, $1640 \times 200 \times 200$ grid points are allocated with uniform width Δ in all directions, where L is the characteristic length scale of the grid panel. Periodic conditions are employed in the two transverse directions (x_2 and x_3). See Fig. 1 for a sketch. The velocity field (U_1, U_2, U_3), density ρ, pressure P and temperature T are normalized by U_∞, ρ_∞, $\rho_\infty U_\infty^2$, T_∞, where the subscript ∞ denotes the dimensional oncoming mean quantities. Two dimensionless parameters are introduced, $M = U_\infty/a_\infty$ and $Re = U_\infty L/\nu_\infty$, where a_∞ and ν_∞ are the sound speed and kinematic viscosity of the oncoming stream.

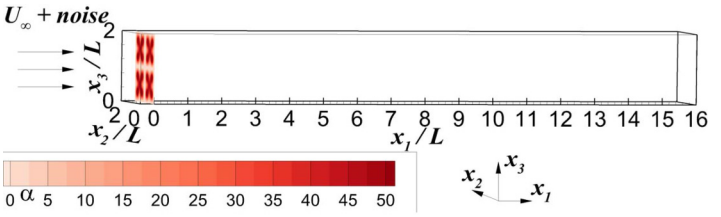

(a)

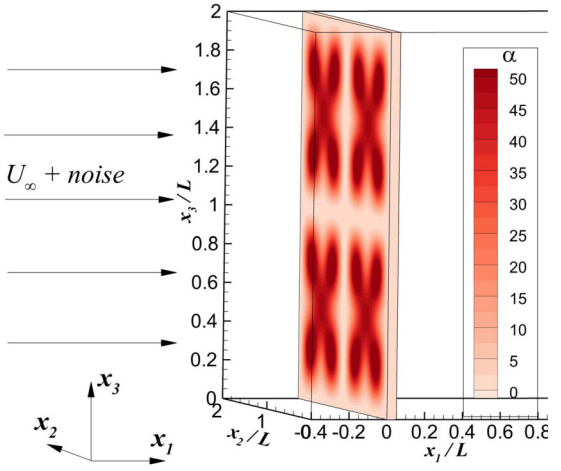

(b)

FIG. 1. Sketch of the computational domain of the two-scale wake. The membrane is highlighted. (a) Global view; (b) zoomed view near inlet.

The dimensionless governing equations for the compressible flow are

$$\frac{\partial \rho}{\partial t} + \frac{\partial (\rho U_k)}{\partial x_k} = 0, \tag{2}$$

$$\frac{\partial (\rho U_i)}{\partial t} + \frac{\partial (\rho U_k U_i)}{\partial x_k} = -\frac{\partial P}{\partial x_i} + \frac{\partial \tau_{ik}}{\partial x_k} - \alpha \rho U_i, \tag{3}$$

$$\frac{\partial E}{\partial t} + \frac{\partial [(E+P)U_k]}{\partial x_k} = \frac{\partial b_k}{\partial x_k} - \frac{1}{2}\alpha \rho U_k U_k, \tag{4}$$

where the total energy E is defined as

$$E = \frac{1}{2}\rho U_k U_k + \frac{\rho T}{\Gamma(\Gamma-1)\mathrm{Ma}^2}, \tag{5}$$

with $\Gamma = 1.4$ the specific heat capacity ratio. The stress tensor and heat flux vector are

$$\begin{aligned} \tau_{ij} &= \frac{\mu}{\mathrm{Re}}\left(\frac{\partial U_i}{\partial x_j} + \frac{\partial U_j}{\partial x_i} - \frac{2}{3}\delta_{ij}\frac{\partial U_k}{\partial x_k}\right), \\ b_i &= U_k \tau_{ik} + \frac{\mu}{\mathrm{PrRe}(\Gamma-1)\mathrm{Ma}^2}\frac{\partial T}{\partial x_i}, \end{aligned} \tag{6}$$

respectively, where δ_{ij} is Kronecker delta, $\mathrm{Pr} = 0.72$ the Prandtl number, and μ the dynamic viscosity determined by the Sutherland law

$$\mu = T^{1.5}\frac{T_S/T_{\mathrm{ref}} + 1}{T + T_S/T_{\mathrm{ref}}}, \tag{7}$$

with $T_{\mathrm{ref}} = 298.15$ K and $T_S = 110.4$ K. Additionally, the equation of the state for a perfect gas determines the relation between P, ρ, and T, namely,

$$P = \rho T/(\Gamma \mathrm{Ma}^2). \tag{8}$$

We arrange a semipermeable membrane panel with unbounded width in the x_2 and x_3 directions in the streamwise range of $0 \leqslant x_1/L \leqslant 0.05$, which is equivalent to introducing a friction term $-\alpha\rho U_i$ on the right-hand side of Eq. (3). In this paper, we choose

$$\alpha = \begin{cases} \frac{25}{2}\{[1-\cos(2\pi x_2/L)][1-\cos(2\pi x_3/L)] & \text{if } 0 \leqslant x_1/L \leqslant 0.05, \\ \quad +[1-\cos(4\pi x_2/L)][1-\cos(4\pi x_3/L)]\}, & \\ 0, & \text{otherwise.} \end{cases} \tag{9}$$

In this model, the friction coefficient varies in the (x_2, x_3) plane with two spatial scales, L and $L/2$. This implies that the wake immediately behind the membrane will include only two dominant Fourier modes, which enables the analytical approximation in the following subsections.

At the inlet of the computational domain, the infinitesimal noises are chosen to be Gaussian, with a standard variation $0.001U_\infty$ in the x_1 direction. A far-field boundary condition [18] is applied at the outlet of the domain, $x_1 = 16L$. The Reynolds number is set as $\mathrm{Re} = 10\,000$, while the Mach number is $\mathrm{Ma} = 0.3$, indicating that the fluid can be approximately considered as incompressible (since the density change due to velocity is correspondingly about 5%) [19]. This simulation is conducted by an in-house compressible finite difference method solver ASTR, which has been verified in various DNS cases [20,21]. A sixth-order compact central scheme [22] is used for the spatial discretization, and a third-order three-step total variation diminishing Runge-Kutta method [23] is used for time advance. The time step is set as 0.0006, determined by using the equation in Sec. 6.2.2 of Ref. [24] with $\mathrm{CFL} = 0.73$.

In order to quantitatively perform the following statistical analysis, we define $\langle\rangle$ as the averaging over time t and both spanwise directions x_2 and x_3. We note that the nature of this treatment, which involves spanwise average, is to consider the two large-scale structures as fluctuations rather than as mean shear. It is acceptable because (1) the present calculation is a simplification of grid-generated turbulence, which is always treated by spanwise averaging, and (2) as will be discussed later, according to the present definition, the skewness S_k will include the information on the asymmetry of large-scale structures and allows the treatment of both laminar and turbulent flows in the same mathematical framework. Accordingly, the velocity fluctuation is defined as $u_i = U_i - \langle U_i\rangle$.

As shown in Fig. 2(a), we define three typical spanwise positions for the convenience of the following statistical analysis, i.e., (L, L), $(L/2, L/2)$, and $(L/2, L)$ in the (x_2, x_3) plane, respectively. They are denoted as positions 1, 2, and 3, respectively. In each of these positions, we calculate the local dissipation scales η at different x_1 locations, and compare them with the grid length Δ as shown in Fig. 2(b). It can be found that the maximum value of Δ/η is about 4.2, which is consistent in magnitude with many existing DNS calculations [25–29] and supports the present mesh resolution. For example, according to the conclusion of Ref. [25], we would expect that the error of first- and second-order statistics is less than 5%, and the error of third- and fourth-order statistics is less than 10% in the present calculation.

B. DNS results

The transition of the flow can be visually illustrated by using the instantaneous velocities. Figure 3 shows the snapshots of streamwise velocity U_1 at different (x_2, x_3) planes; for completeness, the snapshot of U_1 at the $x_2/L = 0.25$ plane [see the dashed line in Fig. 2(a) for a sketch] is

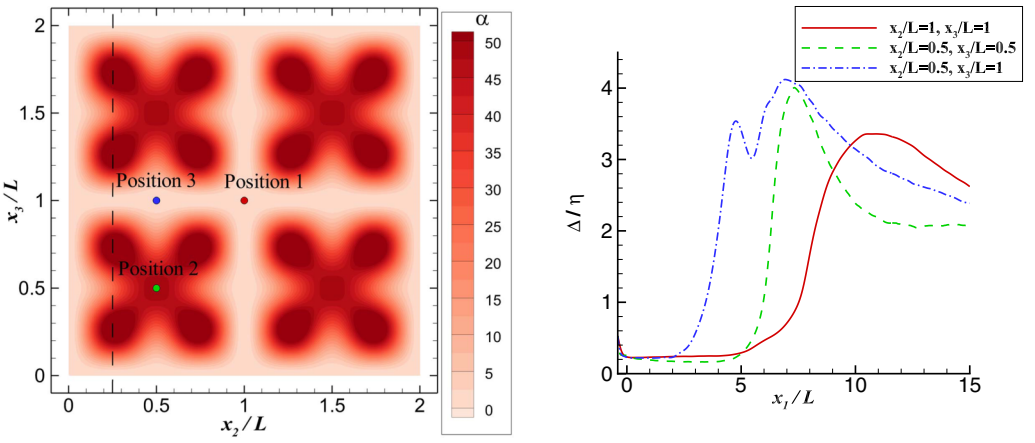

(a) (b)

FIG. 2. Streamwise evolution of Δ/η at different positions in the two-scale wake, respectively. (a) The spanwise positions, denoted as 1, 2, and 3, respectively. The dashed line indicates the location of $x_2/L = 0.25$; (b) streamwise evolution of Δ/η.

shown in Fig. 4. The $x_1/L = 0.05$ plane [Fig. 3(a)] is the location just behind the membrane, while the streamwise velocity is redistributed due to the role of the friction term. The distribution of U_1 is quite similar to the friction coefficient α, which is dominated by structures at two spatial scales L and $L/2$. As will be discussed in Sec. II C, this evolution of velocity redistribution also involves

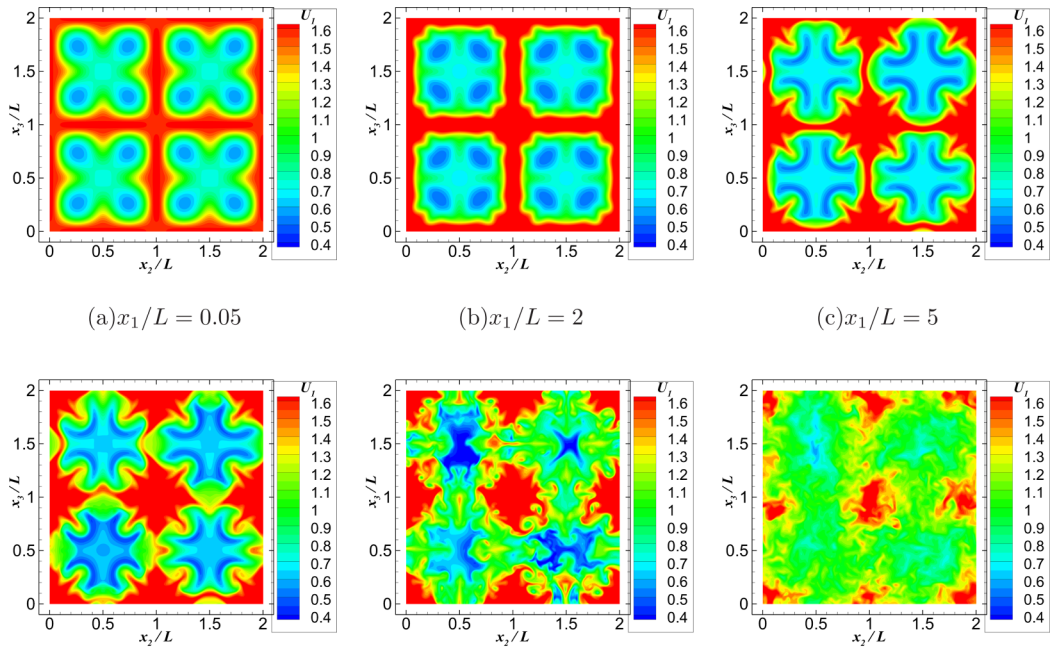

(a)$x_1/L = 0.05$ (b)$x_1/L = 2$ (c)$x_1/L = 5$

(d)$x_1/L = 5.5$ (e)$x_1/L = 6.5$ (f)$x_1/L = 10.5$

FIG. 3. Snapshots of U_1 at different (x_2, x_3) planes in the two-scale wake.

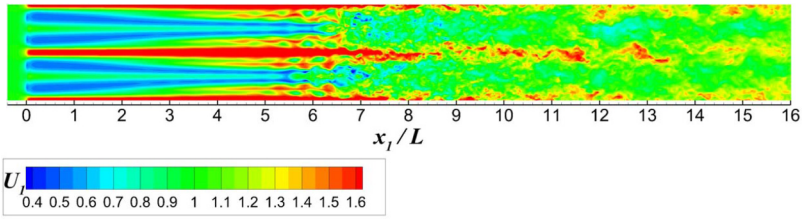

FIG. 4. A snapshot of U_1 at the $x_2/L = 0.25$ plane in the two-scale wake.

spanwise velocities and generates streamwise vortices. Similar to the self-sustaining process in shear flows [30], the streamwise vortices feed the longitudinal streaks due to the lift-up mechanism. In Fig. 4 we can clearly observe these streaklike structures before $x_1/L = 5$. The advection of these streaklike structures in spanwise directions involves more small-scale structures, as shown in Figs. 3(b)–(d). When $x_1/L = 5$ [Fig. 3(c)], slight asymmetry can be observed, indicating that the small-scale perturbations are amplified because of the secondary instability, which is similar as the bypass transition in boundary-layer flows [31]. This instability finally yields turbulent flow structures, as shown in Figs. 3(e) and 3(f). The snapshot of P at the $x_2/L = 0.25$ plane is shown in Fig. 5, where it is clear that there is very weak adverse pressure gradient behind the membrane, while in the early transition region the pressure is quasiconstant.

We present the turbulence intensity I and Taylor-scale Reynolds number Re_λ in Fig. 6. The rapid-increasing region of both them indicates the location of transition, which is about $4 < x_1/L < 7$, in agreement with the snapshots of Figs. 3 and 4.

As introduced in Sec. I, we focus on the skewness of streamwise velocity fluctuation gradient, defined as Eq. (1). As shown in Fig. 7, the value of S_k is positive in the very early evolution before $x_1/L = 3$, then it decreases rapidly to a negative number of about -1.7 and increases to an asymptotic value of about -0.5. This asymptotic value -0.5 is in agreement with traditional turbulence theories [2,4], indicating that the flow can be considered to be fully developed in the region $x_1/L > 7$. Before that, i.e., when $3 < x_1/L < 7$, the trend from decreasing to increasing is similar to Fig. 6 of Ref. [13], which may indicate that the flow in this region has some common properties as the nonequilibrium turbulence [9,14,15]. The most interesting phenomenon here would be the positive values of S_k in the region $x_1/L < 3$, i.e., the zone of early transition. We will introduce an analytical model to approximately explain this phenomenon in the next subsection.

C. A simplified model for explaining the positive S_k

In order to explain the phenomenon of positive S_k, we introduce a simplified model by using the following assumptions for the flow in the early transition stage:

(1) The flow is incompressible and inviscid. This was explained in the last subsection. Specifically, we remark that the inviscid assumption is appropriate since the flow in early transition is out

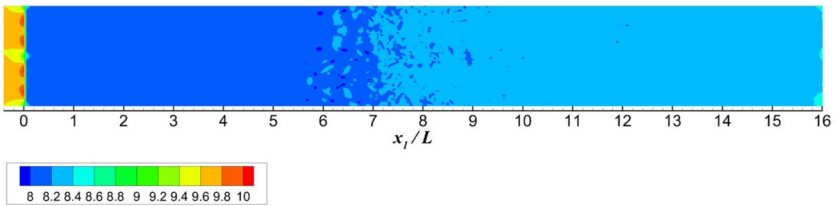

FIG. 5. A snapshot of P at the $x_2/L = 0.25$ plane in the two-scale wake.

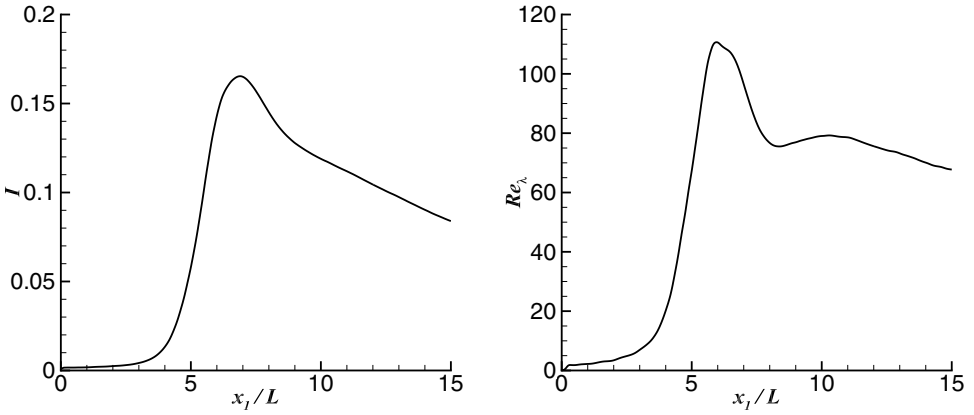

FIG. 6. Streamwise evolution of (a) turbulence intensity I and (b) Taylor-scale Reynolds number Re_λ in the two-scale wake.

of equilibrium, while only advection is dominant. In fact, when the interscale energy transfer is well constructed, the viscosity effect should not be neglected [5,6,32,33].

(2) Symmetry between the x_2 and x_3 directions. This is reasonable since the distribution of α is symmetric.

(3) Similar to Ref. [30], we assume the decoupling between streamwise vortices and streamwise velocity. The underlying reason is that the high- and low-speed structures in early transition are analogous to the streaks in wall flows. This decoupling implies that the streamwise velocity is $U_1(x_1, x_2, x_3, t)$, but the spanwise velocities should be almost independent of x_1 and be written as $U_2(x_2, x_3, t)$ and $U_3(x_2, x_3, t)$, respectively. This assumption is verified in Fig. 8 by showing the spanwise velocities at different x_1 locations. It is observed that the main structures of streamwise

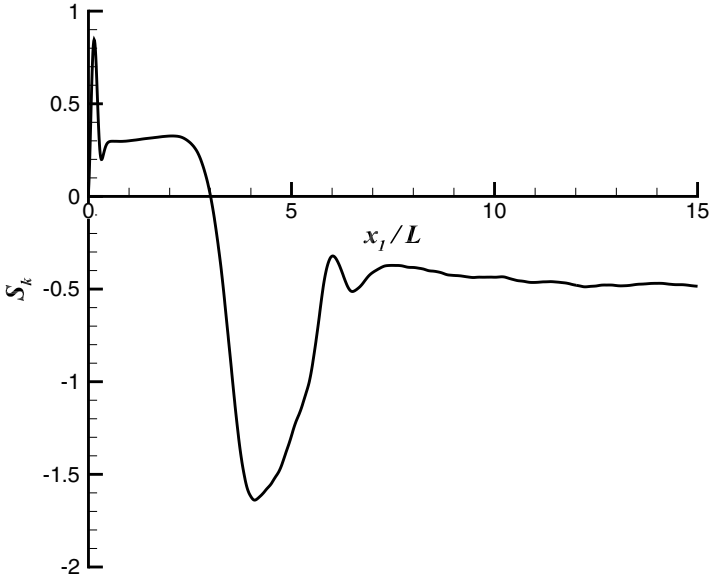

FIG. 7. Streamwise evolution of S_k in the two-scale wake.

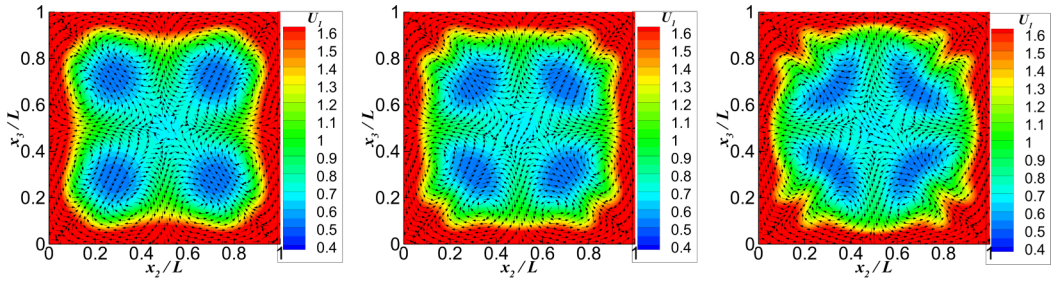

FIG. 8. Spanwise flow structures in the $L \times L$ cell at different x_1 locations in early transition of the two-scale wake, respectively. Arrows indicate the spanwise velocities, while contours are streamwise velocities. (a) $x_1/L = 1$; (b) $x_1/L = 2$; (c) $x_1/L = 3$.

vortices at different x_1 locations are quite similar in Fig. 8, which can be sketched as Fig. 9. The full analytical expression will be discussed later.

(4) We assume that the streamwise velocity U_1 behind the membrane contains only the two largest scales, leading to the velocity profile

$$\begin{aligned} U_1|_{x_1/L\geqslant 0.05} &= a_0 - b[1-\cos(2\pi x_2/L)][1-\cos(2\pi x_3/L)] \\ &\quad - c[1-\cos(4\pi x_2/L)][1-\cos(4\pi x_3/L)] \\ &= a + b\cos(2\pi x_2/L) + b\cos(2\pi x_3/L) - b\cos(2\pi x_2/L)\cos(2\pi x_3/L) \\ &\quad + c\cos(4\pi x_2/L) + c\cos(4\pi x_3/L) - c\cos(4\pi x_2/L)\cos(4\pi x_3/L), \end{aligned} \tag{10}$$

where a_0, a, b, and c are positive and evolute slowly along the streamwise location and $a = a_0 - b - c$, as shown in Fig. 10. The values of b and c correspond to the amplitude of the largest Fourier modes, respectively. To support this assumption, in Fig. 11 we show the streamwise evolution of perturbation energy and $(\partial u_1/\partial x_1)^2$ at different wave numbers, respectively. It is obvious that in the early transition region the first two wave numbers dominate, which correspond to the two-scale distribution of the friction coefficient. Higher wave numbers contain relatively less energy and dissipation, especially in the early transition range, indicating that they could be approximately neglected. According to Eq. (9) we have $b = c$ when $x_1/L = 0.05$, which is verified in Fig. 10. In

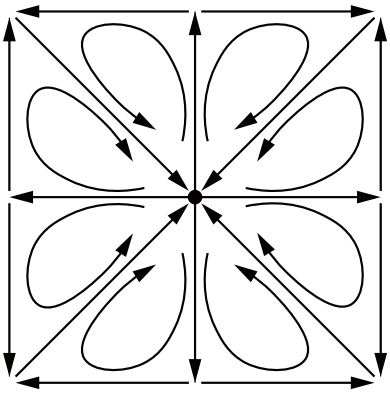

FIG. 9. Sketch of the main structures in the $L \times L$ cell of streamwise vortices in early transition of the two-scale wake. Arrows indicate the flow direction in a streamwise slice.

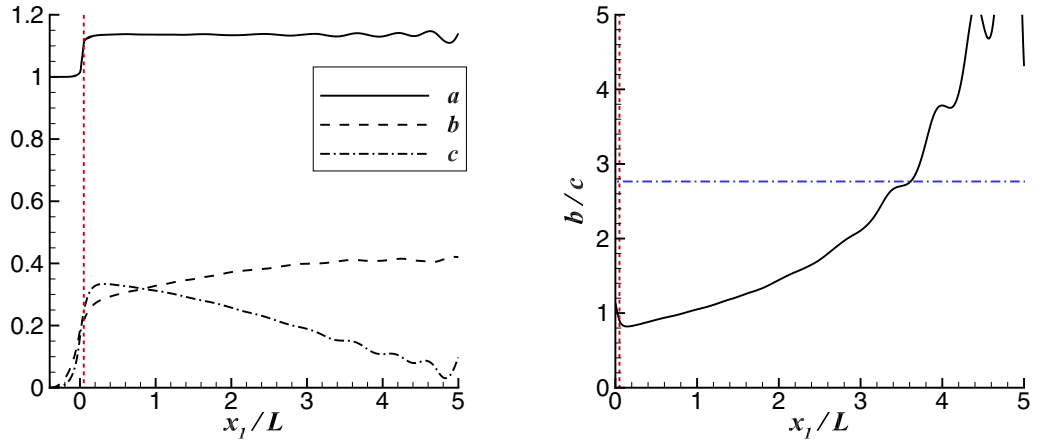

(a) (b)

FIG. 10. The evolution of a, b, c, and b/c along the streamwise direction in the two-scale wake. The red vertical line indicates the location behind the membrane $x_1/L = 0.05$. The blue horizontal line corresponds to $b/c = 2.765$, a critical value for the sign of S_k according to our model.

the interval $0.05 < x_1/L < 5$, The evolution trends of b and c in Fig. 10 are similar to the curves $k = 1$ and $k = 2$ in Fig. 11(a), respectively, since they both describe the energy at large scales. The value of a corresponds to the mean streamwise velocity, which increases from 1 to about 1.12 behind the membrane. This increase corresponds to the weak compressibility. In the early transition stage behind the membrane, it is shown in Fig. 10 that a is quasiconstant due to the zero pressure gradient, indicating the assumption

$$\frac{\partial \langle U_1 \rangle}{\partial x_1} = 0. \tag{11}$$

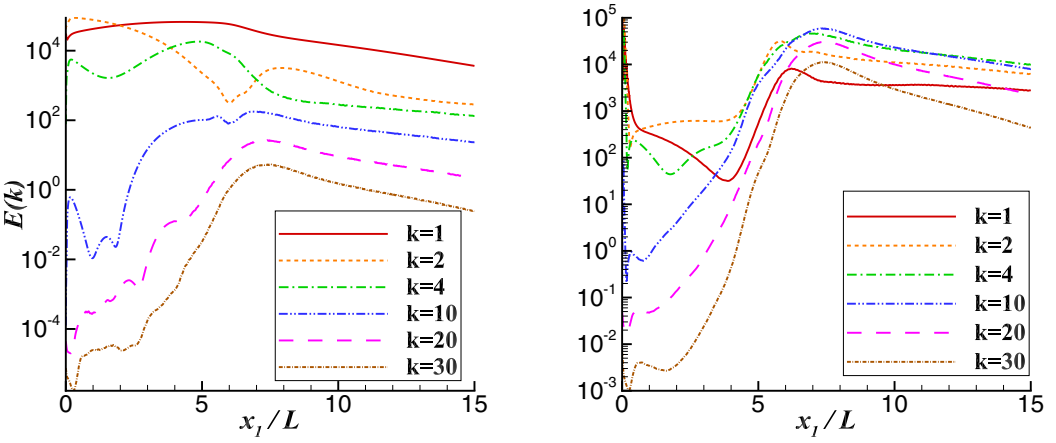

(a) (b)

FIG. 11. Streamwise evolution of (a) kinetic energy and (b) $(\partial u_1/\partial x_1)^2$ at several wave numbers in the two-scale wake. The wave number in normalized by $2\pi/L$.

This assumption is a weak version of Taylor's frozen-flow hypothesis, which has been widely used in experimental studies of grid turbulence [34]. Note that we do not assume constant b or c.

(5) Also, we assume that the velocity profiles of U_2 and U_3 contain only the two largest scales.

To introduce the model in the early transition region, we start from the advection equation

$$U_1\frac{\partial U_1}{\partial x_1}+U_2\frac{\partial U_1}{\partial x_2}+U_3\frac{\partial U_1}{\partial x_3}=0. \tag{12}$$

Comparing to the advection-diffusion equation (1) of Ref. [30], here we neglect the diffusion because of assumption (1). There is no pressure term in Eq. (12) because of the following two facts: (1) As shown in Fig. 5, in the early transition region the pressure is quasiconstant. (2) As discussed in Ref. [30], the pressure effect is not important for the generation of streaks by streamwise vortices (this can be explained by the lift-up mechanism without the attendance of pressure gradient), although it plays a role in the formation of small-scale waves due to instability. Because in the early transition region the instability waves have not been accumulated to finite level, the pressure effect is neglected. From assumption (4), we have locally $\frac{\partial\langle U_1\rangle}{\partial x_1}=0$, hence $\frac{\partial U_1}{\partial x_1}=\frac{\partial u_1}{\partial x_1}$. In addition, in the present case U_1 is always positive at any position in the calculation domain, leading to the relation

$$\mathrm{sgn}(S_k)=\mathrm{sgn}\left\langle\left(U_1\frac{\partial U_1}{\partial x_1}\right)^3\right\rangle=\mathrm{sgn}\left\langle\left(-U_2\frac{\partial U_1}{\partial x_2}-U_3\frac{\partial U_1}{\partial x_3}\right)^3\right\rangle. \tag{13}$$

Here U_1 is assumed to satisfy the expression (10). Therefore, in order to explain the phenomenon of positive S_k, a key question is to write the expressions of spanwise velocities U_2 and U_3.

Following Waleffe [30], the distribution of spanwise velocities should be a solution of the left-hand side of Eq. (6) in Ref. [30]. As a consequence, for $U_2(x_2,x_3,t)$ we write

$$\left(\frac{\partial}{\partial t}-\frac{1}{\mathrm{Re}}\nabla^2\right)\nabla^2U_2(x_2,x_3,t)=0. \tag{14}$$

For the convenience of writing the solutions, we define a coordinate transformation $\xi_2=x_2-L/2$, $\xi_3=x_3-L/2$, and rewrite Eq. (14) as

$$\left(\frac{\partial}{\partial t}-\frac{1}{\mathrm{Re}}\nabla^2\right)\nabla^2U_2(\xi_2,\xi_3,t)=0. \tag{15}$$

Due to periodicity and symmetry (see Fig. 9 for the sketch), $U_2(\xi_2,\xi_3,t)$ should be symmetric with respect to the ξ_3 axis and antisymmetric with respect to the ξ_2 axis. The boundary conditions are

$$U_2(\pm L/2,\xi_3,t)=0. \tag{16}$$

For $U_3(\xi_2,\xi_3,t)$ the description is similar.

On another hand, due to the decoupling with streamwise velocity [assumption (3)], the continuity equation writes

$$\frac{\partial U_2(\xi_2,\xi_3,t)}{\partial\xi_2}+\frac{\partial U_3(\xi_2,\xi_3,t)}{\partial\xi_3}=0. \tag{17}$$

As shown in the Appendix for the derivation details, for all two-scale solutions [assumption (5)] of Eqs. (15) and (17), the only symmetric solution [assumption (2)] should be written as

$$\begin{cases}U_2(\xi_2,\xi_3)=-d\sin(2\pi\xi_2/L)\cos(4\pi\xi_3/L)+\dfrac{d}{2}\sin(4\pi\xi_2/L)\cos(2\pi\xi_3/L),\\ U_3(\xi_2,\xi_3)=-d\sin(2\pi\xi_3/L)\cos(4\pi\xi_2/L)+\dfrac{d}{2}\sin(4\pi\xi_3/L)\cos(2\pi\xi_2/L),\end{cases} \tag{18}$$

with d positive constant. The velocity field is accordingly shown in Fig. 9.

The sign of S_k can be evaluated by substituting Eqs. (10) and (18) into Eq. (13). We obtain

$$\mathrm{sgn}(S_k) = \mathrm{sgn}\left(-bc^2d^3\left[20\left(\frac{b}{c}\right)^2 + 289\frac{b}{c} - 952\right]\right). \tag{19}$$

It is then easy to obtain $S_k > 0$ when $b/c < 2.765$, while $S_k < 0$ when $b/c > 2.765$. In the present DNS case, as shown in Fig. 10, we have $b/c = 1$ just behind the membrane; therefore S_k is positive, corresponding to the phenomenon in DNS.

This result can be further used to predict the streamwise interval for positive S_k. According to Fig. 10(b), the value of b/c increases from 1 to 2.765 in the streamwise interval $x_1/L < 3.8$, which corresponds to positive S_k from the above model. This interval is close to the DNS evidence in Fig. 7, where positive S_k corresponds to about $x_1/L < 3$.

We can remark on the present model from the viewpoint of energy transfer. If the flow is dominated by only two largest scales, the sign of S_k is determined by the ratio of the energies at the two scales, i.e., b/c. If initially the smaller scale contains enough energy, i.e., c is not too small, then b/c can be less than 2.765 and the value of S_k is positive. On the other hand, we know that positive S_k usually indicates the backward energy transfer in turbulence [2,14], thus analogically it is reasonable in the present case that the smaller scale transfers energy towards the larger scale, i.e., c decreases, b increases, and b/c increases. Finally b/c increases to greater than the critical value 2.765, yielding negative S_k, which corresponds to forward energy transfer.

The present model illustrates that the energies, or, e.g., amplitudes, at the two largest scales can affect the sign of S_k. This mechanism will be supported by another different flow example in the next section.

III. TRANSITION IN A TWO-DIMENSIONAL RAYLEIGH-TAYLOR FLOW WITH A DIFFUSE INTERFACE

A. Physical model

In this section, we will show another physical problem to illustrate the phenomenon of positive S_k. The physical model to be studied is a two-dimensional inviscid Rayleigh-Taylor (RT) problem occurring at a diffuse interface of two miscible fluids with different densities (see Ref. [35] for details). The two-dimensional Cartesian coordinate system (x, y) is employed, with the origin o at the interface and x and y perpendicular and parallel to the interface. The positive x is towards the light fluid, so is the acceleration g. The density disparity is characterized by a dimensionless parameter, the Atwood number, which is defined as $A = (\rho_h - \rho_l)/(\rho_h + \rho_l)$, where ρ_h and ρ_l are the densities of the heavy and light fluids, respectively. The length scales (x, y), time t, velocity field $\mathbf{U} = (u, v)$, density ρ, and pressure p are normalized by L_m, $\sqrt{L_m/g}$, $\sqrt{gL_m}$, ρ_h, and $\rho_h g L_m$, respectively, where $L_m = \min[\rho_0^*/(d\rho_0^*/dx^*)]$ is the minimum density gradient scale length, and the asterisk represents the dimensional quantities. The flow is governed by dimensionless Eulerian equations, which are the same as (2) with the body force and viscous terms neglected. Note that the present model is based on the inertial confinement fusion engineering, for which the temperature is extremely high such that all the gas molecules are dissociated. Thus, the perfect-gas model is also employed, but in the equation of the state (8), the ratio of the specific heat Γ is referred to as the adiabatic exponent, with its value being changed to 5/3.

At the beginning, the flow field is a sum of a base flow which satisfies the steady Eulerian equation and an infinitesimal perturbation,

$$(\rho, u, v, p) = (\rho_0, 0, 0, p_0)(x) + \epsilon_0(\exp(-x^2), 0, 0, 0)\cos(ky), \tag{20}$$

where $\epsilon_0 \ll 1$ denotes the initial amplitude of the perturbation, and k the wave number in the direction tangential to the interface. The density and pressure of the base flow are selected as

$$\rho_0(x) = [1 - A\tanh(\delta x)]/(1 + A), \tag{21}$$

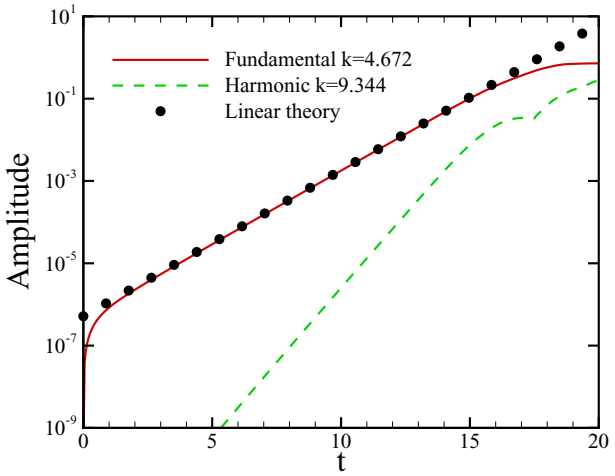

FIG. 12. Evolution of the amplitude of the fundamental ($k = 4.672$) and harmonic ($k = 9.344$) perturbations in the two-dimensional RT flow.

$$p_0(x) = p_c + \int_{x_c}^{x} \rho_0(x)\, dx, \tag{22}$$

where $\delta = A/[2(1 - \sqrt{1 - A^2})]$ is a dimensionless coefficient such that $\min[\rho_0/(d\rho_0/dx)] = 1$ and p_c is a reference pressure at a reference position x_c. For the diffuse interface, δ^{-1} characterizes the thickness of the density-adjustment layer. In this paper, we choose $(p_c, x_c) = (45, -15)$, $A = 0.4$, $\epsilon_0 = 10^{-6}$, and $k = 4.672$, the same as the parameters of case 1 in Ref. [35]. In the simulation, the computational domain is selected as $[-10, 10] \times [0, y_l]$, with 2001×121 grid points employed, where $y_l = 2\pi/k \approx 1.34$.

B. Numerical results

The temporal evolution of the perturbation starting from (20) is obtained by DNS. The amplitude of the fundamental perturbation is shown by the red solid line in Fig. 12. As revealed by Refs. [36,37], the RT instability for a diffuse interface admits an infinite number of discrete eigenmodes with different growth rates. An arbitrarily introduced initial perturbation [the second term on the right-hand side of (20)] is considered as a superposition of all the eigenmodes, whose amplitudes can be obtained by the multimode decomposition as in [35]. At early time instants, $t < 2$, all of these eigenmodes are competing, rendering an algebraic growth of the total amplitude, which was referred to as a prelinear phase. Then the dominant eigenmode (with the greatest growth rate) amplifies exponentially, with its growth rate obtained by the slope of the amplitude curve, 0.817, which agrees with the prediction of the linear stability theory (the black circles). After $t \approx 15$, the amplitude tends to be saturated due to nonlinearity, which is referred to as the nonlinear saturation phase. In this phase, the bubble-spike structure, as shown in Fig. 13, appears and grows. At ever later time instants, the small-scale structures appear due to the Kelvin-Helmholtz instability regime, which eventually leads to transition to turbulent mixing.

The dashed line in Fig. 12 denotes the amplitude of the second-order harmonic perturbation, whose wave number is twice of the fundamental wave number. Before $t = 15$, the harmonic perturbation amplifies exponentially, with the growth rate being about twice of that of the fundamental one.

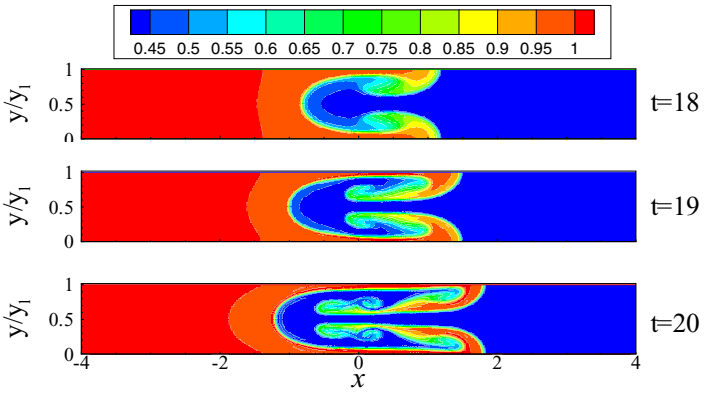

FIG. 13. Contours of the density at $t = 18$, 19 and 20 for the DNS result of the two-dimensional RT flow, respectively.

Since the base flow is stationary, the instantaneous velocity u is also the perturbation to the base flow. We define the ensemble $\langle\rangle$ as the spatial averaging over the y direction. According to Eq. (1), it is easy to see that in the linear phase, for which the perturbation is sinusoidal with a single wave number in y, the skewness is exactly zero. However, if the flow field includes more length scales with moderate amplitudes in the y direction, S_k may be nonzero. Such a situation can occur when a single-mode RT instability evolves to the weakly nonlinear phase, which is almost the most simple setup of the RT instability simulations.

Figure 14 shows the values of S_k in the x-t plane. S_k is exactly zero in the early time, but from $t \approx 11$ to 15, positive skewness can be observed around the interface $x \approx 0$. Intuitively, this should be due to the weakly nonlinear growth of the harmonic mode. As time advances, higher-order harmonics are excited and reach finite amplitude, rendering a more complicated distribution of S_k. Additionally, two strips with negative S_k are located at the edges of the spike and bubble, which expand as time advances.

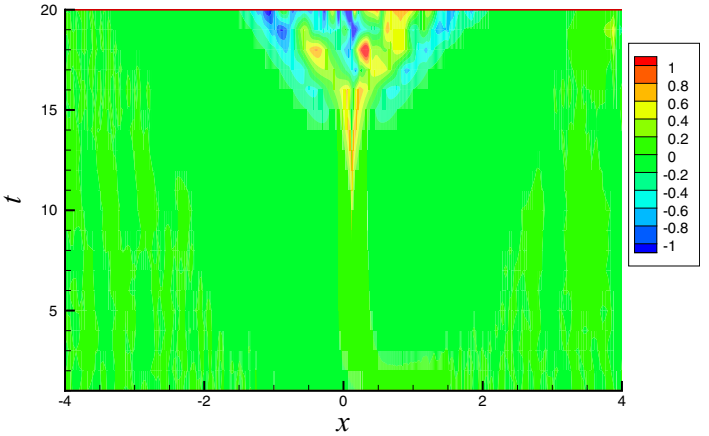

FIG. 14. Contours of the skewness $S_k(x, t)$ in the two-dimensional RT flow.

C. Prediction of the skewness using the weakly nonlinear theory

In the weakly nonlinear phase, when the fundamental mode reaches a finite amplitude, the high-order harmonics are exited in sequence. Now our attention is restricted in the early nonlinear stage, in which only the second-order harmonic mode comes into play, and the feedback from the growth of the harmonic mode to the fundamental one, as well as to the base flow, is negligible. The perturbation field is therefore expressed as

$$\varphi = \varphi_0(x) + \epsilon\hat{\varphi}_1(x)\, e^{\gamma t + i\,ky} + \epsilon^2\hat{\varphi}_2(x,t)\, e^{2\,i\,ky} + \cdots + \text{c.c.}, \tag{23}$$

where $\varphi_0 = (\rho_0, 0, 0, p_0)^T$, $\hat{\varphi} = (\hat{\rho}, \hat{u}, \hat{v}, \hat{p})^T$, $i = \sqrt{-1}$, ϵ is the amplitude of the excited RT instability mode, and c.c. represents the complex conjugate. ϵ can be obtained by the multimode decomposition as in Ref. [35], and for the present configuration, $\epsilon = 1.02\epsilon_0$.

Following Ref. [37], the eigenfunction of the fundamental mode for a high wave number $k \gg 1$ (in the present setup, $k = 4.672$ is already sufficient to be approximated as $k \gg 1$, as proven by Ref. [37]) can be described by the Wentzel-Kramers-Brillouin approximation, and the perturbation velocity $\hat{u}_1$ reads

$$\hat{u}_1 \sim \sin\left(k\int_{x_B}^{x}\sqrt{G_0}\,dx + \frac{\pi}{4}\right), \quad x \in (x_B, x_A), \tag{24}$$

where

$$G_0 = \left(\frac{\rho_0}{p_0\Gamma} - \frac{\rho_0'}{\rho_0}\right)/\gamma^2 - 1, \tag{25}$$

and x_B and x_A are the two zero (turning) points of G_0. For mode-1 perturbation, the most unstable mode,

$$k\int_{x_B}^{x_A}\sqrt{G_0}\,dx = \frac{\pi}{2}. \tag{26}$$

Note that in the regions $x < x_B$ and $x > x_A$, the eigenfunction dampens to zero exponentially. The variations of the base flow ρ_0 and p_0 are much slower than the exponential (sin) behavior of the perturbation. In the following, the analysis will be performed at different local positions with a rather short length scale x, such that the variations of the base flow are negligible.

From the linearized Eulerian equation, we obtain the perturbation pressure, density, and tangential velocity in terms of asymptotic series,

$$\begin{aligned}
\hat{p}_1 &= \frac{\hat{p}_{10}}{k} + \frac{\hat{p}_{11}}{k^2} + O(k^{-3}),\\
\hat{\rho}_1 &= \hat{\rho}_{10} + \frac{\hat{\rho}_{11}}{k} + O(k^{-2}),\\
\hat{v}_1 &= \hat{v}_{10} + \frac{\hat{v}_{11}}{k} + O(k^{-2}),
\end{aligned} \tag{27}$$

where

$$\hat{p}_{10} = -\gamma\rho_0\sqrt{G_0}\cos\Theta, \quad \hat{p}_{11} = -\frac{\gamma\rho_0^2}{\Gamma p_0}\sin\Theta,$$

$$\hat{\rho}_{10} = \frac{1}{\gamma}\left(\frac{\rho_0^2}{\Gamma p_0} - \rho_{0x}\right)\sin\Theta, \quad \hat{\rho}_{11} = \frac{-\gamma\rho_0^2\sqrt{G_0}}{\Gamma p_0}\cos\Theta,$$

$$\hat{v}_{10} = i\sqrt{G_0}\cos\Theta, \quad \hat{v}_{11} = \frac{i\,\rho_0}{\Gamma p_0}\sin\Theta,$$

with $\Theta = k\int_{x_B}^{x}\sqrt{G_0}\,dx + \frac{\pi}{4}$.

The second-order harmonic behaves like

$$\hat{\varphi}(x,t) = \Phi(t)\exp\left(2k\int_{x_B}^{x}\sqrt{G_0}\,dx + \frac{\pi}{2}\right) + \text{c.c.}, \tag{28}$$

where $\Phi = (\Phi_\rho, \Phi_u, \Phi_v, \Phi_p)^T$. Substituting into the Eulerian equations, and collecting the leading-order terms, we obtain

$$\begin{aligned}
\Phi_\rho' + 2\,i\,k\rho_0(\sqrt{G_0}\Phi_u + \Phi_v) + \rho_{0,x}\Phi_u &= -A_1\,e^{2\gamma t},\\
\rho_0\Phi_u' + 2\,i\,k\sqrt{G_0}\Phi_p - \Phi_\rho &= -A_2\,e^{2\gamma t},\\
\rho_0\Phi_v' + 2\,i\,k\Phi_p &= -A_3\,e^{2\gamma t},\\
\Phi_p' + \rho_0\Phi_u + 2\,i\,k\Gamma p_0(\sqrt{G_0}\Phi_u + \Phi_v) &= -\frac{A_4}{k}\,e^{2\gamma t},
\end{aligned} \tag{29}$$

where

$$A_1 = \frac{\rho_0}{2\gamma\Gamma p_0}\left(\frac{\rho_0^2}{\Gamma p_0} - \rho_{0,x}\right),\quad A_2 = \frac{\rho_{0,x}}{4},\quad A_3 = -\frac{\sqrt{G_0}\rho_{0,x}}{4},\quad A_4 = -\frac{i\,\gamma\sqrt{G_0}(1+\Gamma)\rho_0^2}{4\Gamma p_0}.$$

Eliminating $\Phi_{\rho,v,p}$, and noting that $k \gg 1$, we arrive at

$$\Phi_u'' - F_1\Phi_u = F_0\,e^{2\gamma t}, \tag{30}$$

where

$$F_1 = \frac{1}{G_0+1}\left(\frac{\rho_0}{p_0\Gamma} - \frac{\rho_0'}{\rho_0}\right),\quad F_0 = -\frac{A_1 + 2\gamma A_2 - 2A_3\gamma\sqrt{G_0}}{(G_0+1)\rho_0}.$$

Taking into account (25), we obtain

$$F_1 = \gamma^2,\quad F_0 = -\frac{1}{2\gamma\rho_0}\left(\frac{\rho_0}{p_0\Gamma} - \frac{\rho_0'}{\rho_0}\right). \tag{31}$$

Note that F_1 is positive, and F_0 is negative at all positions of our interest. The solution for Φ_u is

$$\Phi_u = \frac{F_0}{3\gamma^2}\,e^{2\gamma t} + C_1\,e^{\gamma t} + C_2\,e^{-\gamma t}, \tag{32}$$

where C_1 and C_2 are constants. We will focus on the particular part with a growth rate of 2γ, as confirmed by the dashed line in Fig. 12.

Now we can express the instantaneous velocity as

$$u = \epsilon\bar{A}\cos(ky) + \epsilon^2\bar{B}\cos(2ky), \tag{33}$$

where $\bar{A} = \sin\Theta\,e^{\gamma t}$ and

$$\bar{B} = (F_0/3\gamma^2)\sin(2\Theta)\,e^{2\gamma t}. \tag{34}$$

Figure 15 plots the eigenprofiles of the fundamental and second-order harmonic perturbations at representative time instants in the weakly nonlinear phase, the simplified profiles (33) are overall

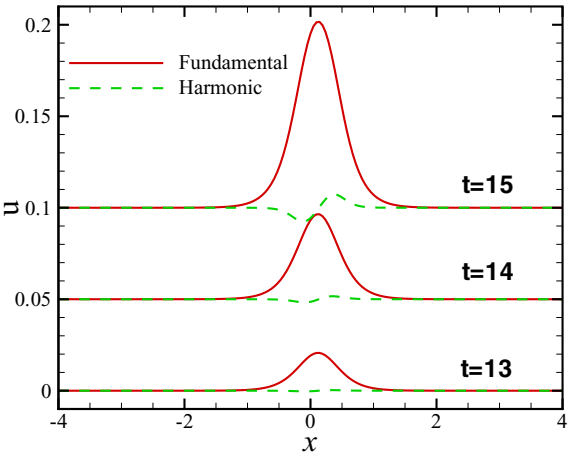

FIG. 15. Eigenprofiles of the fundamental and second-order harmonic perturbations for different t in the two-dimensional RT flow. The curves for $t = 14$ and 15 are shifted for plotting convenience.

confirmed. Then the skewness at a time instant t_0 is expressed as

$$\begin{aligned} S_k(x, t_0) &= \frac{1}{y_l \bar{C}} \int_0^{y_l} \left(\frac{\partial u}{\partial x}\right)^3 dy \\ &= \frac{1}{y_l \bar{C}} \int_0^{y_l} \left[\epsilon \bar{A}_x \cos(ky) + \epsilon^2 \bar{B}_x \cos(2ky)\right]^3 dy \\ &= \frac{1}{y_l \bar{C}} \epsilon^3 \bar{A}_x^2 \bar{B}_x \int_0^{y_l} \cos^2(ky) \cos(2ky)\, dy \\ &= \frac{1}{y_l \bar{C}} \epsilon^3 \bar{A}_x^2 \bar{B}_x \int_0^{y_l} \frac{1}{2} \cos^2(2ky)\, dy = \frac{\epsilon^3 \bar{A}_x^2 \bar{B}_x}{4\bar{C}}, \end{aligned} \tag{35}$$

where the subscript x denotes partial derivative in the x direction, and $\bar{C} > 0$ represents the denominator of S_k. Because $\bar{A}_x^2$ and $\bar{C}$ are non-negative, the sign of S_k depends only on the behavior of $\bar{B}_x$. It is obtained from (34) that

$$\mathrm{sgn}[\bar{B}_x] = \mathrm{sgn}[\frac{2F_0\sqrt{G_0}k}{3\gamma^2} \cos(2\Theta)] = \mathrm{sgn}[-\cos(2\Theta)]. \tag{36}$$

In the interval of our interest, $x \in (x_B, x_A)$, because the cos function changes its phase from $\pi/2$ to $3\pi/2$, which is always negative, $\bar{B}_x$ is positive, so is the skewness S_k. However, in the regions $x < x_B$ and $x > x_A$, S_k could become negative. As shown in Fig. 14, in the weakly nonlinear phase, $10 < t < 15$, S_k is positive around the interface $x = 0$, but negative in the outer regions, $x < x_B$ and $x > x_A$. This is exactly in agreement with the above theoretical predictions.

Figure 16 further compares the theoretical prediction of the skewness with the numerical results for different time instants, $t = 11$, 13, and 14, where the skewness is normalized by its maximum value $S_{k,\max} = \max_x(S_k)$. The distributions of different curves around the interface $x = 0$ agree well, confirming our weakly nonlinear analysis. Note that the distributions of $\bar{A}_x^2$ and $\bar{C}$ are quite similar, the normalized skewness can be approximated by $S_k/S_{k,\max} \approx \bar{B}_x/\max_x(\bar{B}_x)$, confirming the significance of $\bar{B}_x$ on predicting the sign of S_k. In later times, the single-peak distribution of S_k is replaced by a multipeak distribution, due to the excitation of higher-order harmonics, which is not shown, however, because it is unrelated to our topic.

We remark that the present model shows the similar mechanism for the phenomenon of positive S_k as the two-scale wake case. Here the relation of the amplitudes of harmonic mode is much smaller

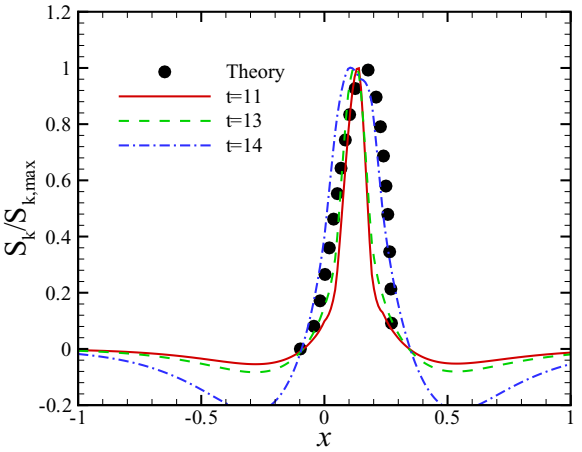

FIG. 16. Comparison of normalized skewness by its maximum value, $S_k/S_{k,\max}$, between the theoretical prediction and the simulation results.

than the fundamental mode, characterized by $\bar{B}_x$, is found to be the main origin of the positive S_k phenomenon in Eq. (36). In the next section we will give more explanations and perspectives.

IV. CONCLUDING REMARKS

In the statistical point of view, the skewness of the longitudinal velocity gradient S_k is usually related to energy transfer in turbulence; for example, the Kolmogorov forward energy cascade in fully developed turbulence implies negative S_k, while Gaussian random noise and infinitesimal perturbations lead to zero S_k. In this sense, revealing more about the evolution of S_k will be helpful for understanding the formation of the equilibrium turbulence, which is undoubtedly a key unclear question till now. In the present contribution, we have shown by two DNS cases that, in the early transition stage, S_k can be positive, in contrast to the energy cascade in equilibrium turbulence.

Two analytical models, introduced in Secs. II C and III C, can predict the phenomenon of positive S_k, which is in good agreement with the DNS results. Both models assume that the flow is constituted by only two dominant Fourier modes with harmonic relations. Although this is a very simple simplification, the phenomenon of positive S_k is well captured. Both analytical models show that S_k can be positive or negative, according to the different interactions between these two Fourier modes. In both flows, the sign of S_k is attributed to the amplitudes of the largest modes. We remark that this does not mean that the relation of amplitudes is the only mechanism. In fact, the effect of amplitudes was obtained by fixing the relation of velocity phases in the present paper. For example, the distribution function (9) of α implies that the velocity phases at the two largest scales are aligned. We will show that the phase relation can also affect the sign of S_k. Taking a two-dimensional flow as an example, if the longitudinal velocity component u_1 can be expressed in terms of Fourier series, i.e., $u_1(\vec{x}) = \sum_{\vec{k}} e^{i\vec{k}\cdot\vec{x}} a_1(\vec{k}) e^{i\phi_1(\vec{k})} + \text{c.c.}$, simple derivations will lead to the expression

$$\left\langle \left(\frac{\partial u_1}{\partial x_1} \right)^3 \right\rangle = \sum_{\vec{k}=\vec{p}+\vec{q}} k_1 p_1 q_1 a_1(\vec{k}) a_1(\vec{p}) a_1(\vec{q}) \sin[\phi_1(\vec{p}) + \phi_1(\vec{q}) - \phi_1(\vec{k})]. \tag{37}$$

Here a_1 is the amplitude, and ϕ_1 is the phase. In particular, a triad phase, $\phi_1(\vec{p}) + \phi_1(\vec{q}) - \phi_1(\vec{k})$, is explicitly represented on the right-hand side, indicating the link between S_k and the phase of velocities (see Refs. [11,38–40] for more discussions). This expression explicitly illustrates that

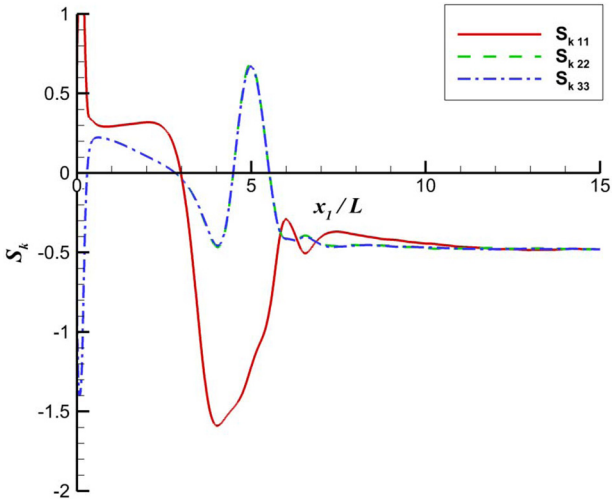

FIG. 17. Evolution of the the skewness values of $\partial u_1/\partial x_1$, $\partial u_2/\partial x_2$, and $\partial u_3/\partial x_3$ in the two-scale wake, respectively.

both the amplitudes and the phases can affect the evolution of S_k. Considering the coupling of the phase evolution and amplitude, the related analysis will be much more complicated and is expected to be investigated in the future.

In addition, we remark that the present evidence and analysis are still not sufficient to assert that the skewness is positive in all situations, because laminar-turbulent transition could be triggered by more types of boundary conditions and initial perturbations. However, the value of our finding is to stimulate further observations of S_k in future transition studies in order to confirm the universality of the emergence of positive S_k. Since the positive S_k is a direct consequence of the nonlinear interaction of different Fourier modes, which is considered as the early fingerprint of transition, a new criterion for determining the transition onset may be constructed by observation of S_k, which is superior to the skin-friction coefficient c_f as in many engineering applications because the former is easier to be measured experimentally.

Finally, we comment that although the present study considers only the skewness of the longitudinal component of velocity gradient in the streamwise direction, the anisotropy of the sixth-order velocity gradient tensor, $\langle \frac{\partial u_i}{\partial u_j} \frac{\partial u_k}{\partial u_l} \frac{\partial u_m}{\partial u_n} \rangle$, is an interesting topic [41]. For example, in the two-scale wake case, we can calculate more longitudinal components and show the values of the skewness of $\partial u_1/\partial x_1$, $\partial u_2/\partial x_2$, and $\partial u_3/\partial x_3$ (denoted as S_{k11}, S_{k22}, and S_{k33}, respectively) in Fig. 17. The curves of S_{k22} and S_{k33} coincide because of symmetry. Although the values of S_{k22} and S_{k33} are not equal to S_{k11}, it is interesting that they have some qualitative similarities: (1) In the region of $x_1/L > 12$ the values of skewness coincide, because there is no large-scale shear structure and the flow is quasi-isotropic. We remark that even in anisotropic flows, the skewness of streamwise velocity gradient might also be approximately used together with the Karman-Howarth equation of isotropic turbulence. For example, in Ref. [42] the subgrid-scale model is derived with local isotropy assumption, but the longitudinal direction is specifically selected as the streamwise direction in channel flow (see Fig. 12 of Ref. [42]). This indicates that the skewness of streamwise velocity gradient is, at least, a characteristic quantity in anisotropic flows. (2) Similar to S_{k11}, the values of S_{k22} and S_{k33} are positive in most of the early transition region ($0.05 < x_1/L < 3$), although the exact values are not the same. We then expect that these interesting facts can inspire future studies on the anisotropy of the sixth-order velocity gradient tensor in anisotropic flows.

ACKNOWLEDGMENTS

We are grateful to J. Fang for providing the DNS code of the two-scale wake, and to H. Xu and W. Bos for helpful discussions. This work is supported by the National Natural Science Foundation of China (Grants No. 11772032, No. 51976006, No. U20B2003, and No. 11772224).

APPENDIX: DETAILS FOR OBTAINING THE SPANWISE VELOCITIES (18)

We want to find the variable separation solutions of Eq. (15) with boundary condition (16), written as $U_2(\xi_2,\xi_3,t)=A(\xi_2,\xi_3)T(t)$. Moreover, we assume that $\nabla^2 A$ can also be written in variable separation form, i.e., $\nabla^2 A = Y(\xi_2)Z(\xi_3)$.

Solving these equations by using the variable separation method, we obtain the following nontrivial solutions corresponding to a temporal evolution rate $T(t)=\exp(-\lambda t/\mathrm{Re})$:

$$\begin{aligned}A(\xi_2,\xi_3)=&\sum_i C_{1i}\sin\left(2k_{1i}\pi\frac{\xi_2}{L}\right)\cosh\left(2k_{1i}\pi\frac{\xi_3}{L}\right)\\&+\sum_i C_{2i}\sin\left(2k_{2i}\pi\frac{\xi_2}{L}\right)\cos\left(\sqrt{\lambda-4k_{2i}^2\pi^2/L^2}\xi_3\right)\\&+C_3\left[\frac{\sin\left(\sqrt{\lambda}\xi_2\right)}{\sin\left(\sqrt{\lambda}L/2\right)}-\frac{2\xi_2}{L}\right]\\&+C_4\left[\frac{\sinh\left(\sqrt{\lambda}\xi_2\right)}{\sinh\left(\sqrt{\lambda}L/2\right)}-\frac{2\xi_2}{L}\right]\cos\left(\sqrt{\lambda}\xi_3\right)\\&+\sum_i C_{5i}\left[\frac{\sin\left(\sqrt{\lambda+p_i}\xi_2\right)}{\sin\left(\sqrt{\lambda+p_i}L/2\right)}-\frac{\sin\left(\sqrt{p_i}\xi_2\right)}{\sin\left(\sqrt{p_i}L/2\right)}\right]\cosh\left(\sqrt{p_i}\xi_3\right),\end{aligned}\tag{A1}$$

with $k_{1i}, k_{2i}\in\mathbb{N}^+$, $C_\bullet\in\mathbb{R}$, and $\lambda, p_i\in\mathbb{R}\backslash\{0\}$. Using the continuity equation (17), we can calculate the distribution of U_3. Considering the boundary condition for U_3, a similar expression to (16), all possible solutions for A are

$$\begin{aligned}A(\xi_2,\xi_3)=&\sum_i C_{2i}\sin\left(2k_{2i}\pi\frac{\xi_2}{L}\right)\cos\left(\sqrt{\lambda-4k_{2i}^2\pi^2/L^2}\xi_3\right)\\&+C_4\left[\frac{\sinh\left(\sqrt{\lambda}\xi_2\right)}{\sinh\left(\sqrt{\lambda}L/2\right)}-\frac{2\xi_2}{L}\right]\cos\left(\sqrt{\lambda}\xi_3\right)\\&+\sum_i C_{5i}\left[\frac{\sin\left(\sqrt{\lambda+p_i}\xi_2\right)}{\sin\left(\sqrt{\lambda+p_i}L/2\right)}-\frac{\sin\left(\sqrt{p_i}\xi_2\right)}{\sin\left(\sqrt{p_i}L/2\right)}\right]\cosh\left(\sqrt{p_i}\xi_3\right),\end{aligned}\tag{A2}$$

with either

$$C_4\neq 0,\qquad \lambda-4k_{2i}^2\pi^2/L^2=4n_{1i}^2\pi^2/L^2,\quad \lambda=4n_2^2\pi^2/L^2,\quad p_i=-4n_{3i}^2\pi^2/L^2,\quad \forall i$$

or

$$C_4=0,\qquad \lambda-4k_{2i}^2\pi^2/L^2=4n_{1i}^2\pi^2/L^2,\quad p_i=-4n_{3i}^2\pi^2/L^2,\quad \forall i,$$

where $n_{1i}, n_2, n_{3i}\in\mathbb{N}^+$. Following Waleffe [30], we further assume that the temporal evolution is relatively weak, such that the flow can be written as a locally steady form. From assumption (5) we focus on the two largest scales, and thus we take the Fourier transform and perform large-scale truncation on these possible solutions. All possible solutions for U_2 are therefore

$$U_2(\xi_2,\xi_3)=C_{21}\sin(2\pi\xi_2/L)\cos(4\pi\xi_3/L)+C_{22}\sin(4\pi\xi_2/L)\cos(2\pi\xi_3/L),\tag{A3}$$

which corresponds to $k_{21} = 1$, $k_{22} = 2$, and $\lambda = 20\pi^2/L^2$ in Eq. (A2).

We further use the continuity equation (17) to calculate U_3, and compare the expression between U_2 and U_3, respectively. Due to assumption (2), the expressions of U_2 and U_3 should be symmetric, leading to the only final expression (18).

[1] A. N. Kolmogorov, The local structure of turbulence in incompressible viscous fluid for very large Reynolds number, Proc. Math. Phys. Sci. **30**, 301 (1941).

[2] W. J. T. Bos, L. Chevillard, J. F. Scott, and R. Rubinstein, Reynolds number effect on the velocity increment skewness in isotropic turbulence, Phys. Fluids **24**, 015108 (2012).

[3] G. K. Batchelor, *The Theory of Homogeneous Turbulence* (Cambridge University Press, Cambridge, 1953).

[4] C. W. Van Atta and R. A. Antonia, Reynolds number dependence of skewness and flatness factors of turbulent velocity derivatives, Phys. Fluids **23**, 252 (1980).

[5] F. Thiesset, R. A. Antonia, and L. Djenidi, Consequences of self-preservation on the axis of a turbulent round jet, J. Fluid Mech. **748**, R2 (2014).

[6] S. L. Tang, R. A. Antonia, L. Djenidi, and Y. Zhou, Transport equation for the isotropic turbulent energy dissipation rate in the far-wake of a circular cylinder, J. Fluid Mech. **784**, 109 (2015).

[7] L. Djenidi and R. A. Antonia, Modelling the third-order velocity structure function in the scaling range at finite Reynolds numbers, in *22nd Australasian Fluid Mechanics Conference AFMC2020, 6–10* December (Brisbane, Australia, 2020).

[8] R. H. Kraichnan, Inertial ranges in two-dimensional turbulence, Phys. Fluids **10**, 1417 (1967).

[9] F. Liu, L. P. Lu, and L. Fang, Non-equilibrium turbulent phenomena in transitional channel flows, J. Turbul. **19**, 731 (2018).

[10] L. Fang, T. Wu, and W. J. T. Bos, Staircase scaling of short-time energy transfer in turbulence, J. Turbul. **21**, 234 (2020).

[11] J. Chai, T. Wu, and L. Fang, Single-scale two-dimensional-three-component generalized-Beltrami-flow solutions of incompressible Navier-Stokes equations, Phys. Lett. A **384**, 126857 (2020).

[12] L. Fang, W. J. T. Bos., L. Shao, and J.-P. Bertoglio, Time-reversibility of Navier-Stokes turbulence and its implication for subgrid scale models, J. Turbul. **13**, N3 (2012).

[13] L. Fang, Y. Zhu, Y. W. Liu, and L. P. Lu, Spectral non-equilibrium property in homogeneous isotropic turbulence and its implication in subgrid-scale modeling, Phys. Lett. A **379**, 2331 (2015).

[14] F. Liu, L. P. Lu, W. J. T. Bos, and L. Fang, Assessing the nonequilibrium of decaying turbulence with reversed initial fields, Phys. Rev. Fluids **4**, 084603 (2019).

[15] R. J. Hearst and P. Lavoie, Velocity derivative skewness in fractal-generated, non-equilibrium grid turbulence, Phys. Fluids **27**, 071701 (2015).

[16] J. C. Isaza, R. Salazar, and Z. Warhaft, On grid-generated turbulence in the near- and far field regions, J. Fluid Mech. **753**, 402 (2014).

[17] L. Fang, H. K. Zhao, L. P. Lu, Y. W. Liu, and H. Yan, Quantitative description of non-equilibrium turbulent phenomena in compressors, Aerosp. Sci. Technol. **71**, 78 (2017).

[18] J. W. Kim and D. J. Lee, Generalized characteristic boundary conditions for computational aeroacoustics, part 2, AIAA J. **42**, 47 (2004).

[19] J. D. Anderson, *Fundamentals of Aerodynamics*, 4th ed. (McGraw-Hill, New York, 2007).

[20] J. Fang, Y. F. Yao, Z. R. Li, and L. P. Lu, Investigation of low-dissipation monotonicity-preserving scheme for direct numerical simulation of compressible turbulent flows, Comput. Fluids **104**, 55 (2014).

[21] J. Fang, Y. F. Yao, A. A. Zheltovodov, Z. R. Li, and L. P. Lu, Direct numerical simulation of supersonic turbulent flows around a tandem expansion-compression corner, Phys. Fluids **27**, 125104 (2015).

[22] S. K. Lele, Compact finite difference schemes with spectral-like resolution, J. Comput. Phys. **103**, 16 (1992).

[23] S. Gottlieb and C.-W. Shu, Total variation diminishing Runge-Kutta schemes, Math. Comput. **67**, 73 (1998).
[24] N. A. Adams and K. Shariff, A high-resolution hybrid compact-ENO scheme for shock-turbulence interaction problems, J. Comput. Phys. **127**, 27 (1996).
[25] S. Laizet, J. Nedić, and J. C. Vassilicos, Influence of the spatial resolution on fine-scale features in DNS of turbulence generated by a single square grid, Int. J. Comut. Fluid Dyn. **29**, 286 (2015).
[26] Y. Zhou and J. C. Vassilicos, Related self-similar statistics of the turbulent/non-turbulent interface and the turbulence dissipation, J. Fluid Mech. **821**, 440 (2017).
[27] S. C. Tao and Y. Zhou, Turbulent flows around side-by-side cylinders with regular and multiscale arrangements, Phys. Rev. Fluids **4**, 124602 (2019).
[28] S. Laizet, J. C. Vassilicos, and C. Cambon, Interscale energy transfer in decaying turbulence and vorticity-strain-rate dynamics in grid-generated turbulence, Fluid Dyn. Res. **45**, 061408 (2013).
[29] Y. Zhou, K. Nagata, Y. Sakai, H. Suzuki, Y. Ito, O. Terashima, and T. Hayase, Relevance of turbulence behind the single square grid to turbulence generated by regular- and multiscale-grids, Phys. Fluids **26**, 075105 (2014).
[30] F. Waleffe, On a self-sustaining process in shear flows, Phys. Fluids **9**, 883 (1997).
[31] A. Zhang, M. Dong, and Y. Zhang, Receptivity of secondary instability modes in streaky boundary layers, Phys. Fluids **30**, 114102 (2018).
[32] S. L. Tang, R. A. Antonia, L. Djenidi, H. Abe, T. Zhou, L. Danaila, and Y. Zhou, Transport equation for the mean turbulent energy dissipation rate on the centreline of a fully developed channel flow, J. Fluid Mech. **777**, 151 (2015).
[33] R. A. Antonia, S. L. Tang, L. Djenidi, and L. Danaila, Boundedness of the velocity derivative skewness in various turbulent flows, J. Fluid Mech. **781**, 727 (2015).
[34] J. Wyngaard and S. Clifford, Taylor's hypothesis and high-frequency turbulence spectra, J. Atmos. Sci. **34**, 922 (1977).
[35] Z. F. Fan and M. Dong, Multiple eigenmodes of the Rayleigh-Taylor instability observed for a fluid interface with smoothly varying density. III. Excitation and nonlinear evolution, Phys. Rev. E **101**, 063103 (2020).
[36] C. X. Yu, C. Xue, J. Liu, X. Y. Hu, Y. Y. Liu, W. H. Ye, L. F. Wang, J. F. Wu, and Z. F. Fan, Multiple eigenmodes of the Rayleigh-Taylor instability observed for a fluid interface with smoothly varying density, Phys. Rev. E **97**, 013102 (2018).
[37] M. Dong, Z. F. Fan, and C. X. Yu, Multiple eigenmodes of the Rayleigh-Taylor instability observed for a fluid interface with smoothly varying density. II. Asymptotic solution and its interpretation, Phys. Rev. E **99**, 013109 (2019).
[38] M. Buzzicotti, B. P. Murray, L. Biferale, and M. D. Bustamante, Phase and precession evolution in the Burgers equation, Eur. Phys. J. E **39**, 34 (2016).
[39] B. P. Murray and M. D. Bustamante, Energy flux enhancement, intermittency and turbulence via fourier triad phase dynamics in the 1-D Burgers equation, J. Fluid Mech. **850**, 624 (2018).
[40] T. Wu, L. Fang, and Z. Wang, Exact time scale of energy exchange in triad interactions of homogeneous isotropic turbulence, Phys. Fluids **33**, 035136 (2021).
[41] F. H. Champagne, The fine-scale structure of the turbulent velocity field, J. Fluid Mech. **86**, 67 (1978).
[42] G. X. Cui, H. B. Zhou, Z. S. Zhang, and L. Shao, A new dynamic subgrid eddy viscosity model with application to turbulent channel flow, Phys. Fluids **16**, 2835 (2004).